NiO / Sr doped $Ce_{0.85}Pr_{0.10}$ $Er_{0.05}O_{2-\delta}$ mesoarchitectured catalyst for partial oxidation of CH_4 and anode fueled by H_2

Laura Navarrete [a], Mihaela Florea [b,c], Petre Osiceanu [d], Jose Maria Calderon-Moreno [d], Mihaela M. Trandafir [b,c], Simona Somacescu [d,*], Jose Manuel Serra [a,**]

[a] *Instituto de Tecnología Química, (Universidad Polit´ecnica de Valencia - Consejo Superior de Investigaciones Científicas),46022, Valencia, Spain*

[b] *Department of Organic Chemistry, Biochemistry and Catalysis,University of Bucharest, Faculty of Chemistry, Bdul. Regina Elisabeta, 4-12, Bucharest, Romania*

[c] *National Institute of Materials Physics, 405 A, Atomistilor Street, 077125, Bucharest, Romania*

[d] *"Ilie Murgulescu" Institute of Physical Chemistry, Romanian Academy, 060021, Bucharest, Romania*

ARTICLE INFO

Keywords:
Mesoporous
Catalyst
Oxidation of methane
IT-SOFC anode

ABSTRACT

Our study focuses on an advanced exploratory research based on the development of the new IT-SOFCs anode compositions in conjunction with surfactants as template to obtain mesoarchitectured catalysts. We designed NiO/Sr doped $Ce_{0.85}Pr_{0.10}$ $Er_{0.05}O_{2-o}$- (2.5 and 5 mol.% Sr) mesoarchitectures with robust crystalline framework following a hydrothermal synthesis route. NiO was deposited by wet impregnation and calcined in air at 900 °C, in order to assure a good interaction between Ni and mesoporous matrix. The obtained materials exhibit a cubic CeO_2 fluorite phase with Pr_2O_3 and $SrCeO_3$ as secondary phase traces and these were assessed as catalyst for the partial oxidation of CH_4 over time and IT-SOFCs anode under reducing atmosphere. The electrochemical behavior as anode fed by wet H_2 (2.5% vol. H_2O) was investigated in the NiO/CPS/YSZ/GDC/Pt electrochemical cells. The compositional effect on the structural properties, surface chemistry, catalytic and electrochemical performance were highlighted. Sr incorporated in the lattice, proved by X-ray Photoelectron Spectroscopy, guarantees an excellent stability of the catalysts over time for 20h, during partial oxidation of CH_4 with high CH_4 conversion and CO selectivity (90% in the range 700–800 °C) as well as a better performance as IT-SOFCs anode.

1. Introduction

Developing highly efficient and cost-effective anodes for IT-SOFCs is a tremendous challenge of these days, due to increasing worldwide energetic demands in the last decades and stringent regulations in the field of environmental protection to minimizes green-house gas emissions. Solid oxide fuel cells (SOFC) offer a promising way of converting chemical energy into electrical energy with greater efficiency. They operate at elevated temperature (550–1000 °C) to ensure adequate ionic and/or electronic conductivity in electrodes and electrolyte: electrical output is obtained when fuel is provided to the anode side of the cell and air (oxygen) is provided to the cathode. Therefore, the challenge for any material scientist in this field is to design a solid material that will allow oxide-ion conduction at a low enough temperature to be technically useful. The anode materials must meet several stringent criteria to achieve reliable, high and constant performances. The materials selection for a SOFC anode is determined by a number of factors, as a good electronic and ionic conductivity, electrocatalytic activity which is in turn proportional to the surface area (available for the partial electrochemical reaction with gas species), a good porosity for the diffusion of the reactants, a crystalline structure thermally stable, and chemical stability and compatibility between components. Ceria is a widely used compound for different catalytic and fuel cell applications [1–4]. In the last decade, efforts have been focused on the incorporation of different dopants in the fluorite structure, in order to investigate the role of the different dopants and amounts, on the morphology, conductivity and electrocatalytic activity of those materials for their application as electrodes in SOFCs [5,6].

Development of anode materials for a solid-oxide fuel cell (SOFC) that operates at intermediate temperature represents a major challenge

* Corresponding author. Catalysis and Surface Chemistry Lab, "Ilie Murgulescu" Institute of Physical Chemistry, Romanian Academy, Spl. Independentei 202, Bucharest, 060021, Romania..

** Corresponding author.

E-mail addresses: ssimona@icf.ro (S. Somacescu), jmserra@itq.upv.es (J.M. Serra).

URL: http://www.icf.ro/groups/xps/index.html (S. Somacescu).

of these days. At intermediate temperatures the high electrode overpotential as well as the increased resistance of electrolyte still remain shortcomings for this kind of fuel cells. The overcoming could be realized by using an electrolyte with a decreased thickness or using an electrolyte with high ionic conductivity such as cerates [7] type. Due to their tunable ionic conduction behavior, high oxygen storage capacity and the satisfactory thermal and mechanical resistance, doped-CeO_2 materials have been widely studied as component of SOFC directly operated with hydrocarbon fuels. Moreover, rare-earth doped ceria materials were extensively studied [8,9]. In this context, the influence of dopant type and concentration on the catalytic and electrochemical behaviour of ceria-based materials has become an important research field. A very important aspect is related to the improvement of the anode performance by using the mixed conducting oxides. Concerning the composition, different approaches were developed for obtaining nickel based anodes with enhanced carbon tolerance, for fuel cells fed by hydrocarbons. Thus, the addition of the noble metals (e.g. Ru, Au, Pt) to promote the hydrocarbons reforming, could be considered an alternative, but unfortunately these anodes are not economically attractive due to high costs [10–12]. A superior electrochemical performance and high carbon resistance were obtained by incorporation of the cheap materials in the Ni-based anodes, such as TiO_2 [13] and CaO [14].

In the industry, CH_4 is chemically transformed into syngas to produce basic chemicals. Diverse ratios of H_2/CO are obtained depending on the selected synthesis route [15–17]:

Dry reforming: $CH_4 + CO_2 \rightarrow 2H_2 + 2CO\ \Delta H^{\circ} = 247\ kJ\ mol^{-1}$

Steam reforming: $CH_4 + H_2O \rightarrow 3H_2 + CO\ \Delta H^{\circ} = 206\ kJ\ mol^{-1}$

Partial Oxidation: $CH_4 + 1/2\ O_2 \rightarrow 2H_2 + CO\ \Delta H^{\circ} = 36\ kJ\ mol^{-1}$

The syngas (H_2 and CO) is widely employed in the chemical industry for the methanol synthesis or the Fischer–Tropsch process [18]. For that purpose, the most suitable ratio of H_2 to CO is 2, and the catalytic partial oxidation of methane (ĊPOM) in the only one that fulfill that condition and does not need to be adjusted with additional gases. In addition, the steam (SR) and dry (DR) reforming reactions are endothermically activated, thus, external heat exchange is required, whereas the reaction of the ĊPOM is a mildly exothermic and it is more energetically efficient.

For the total conversion of CH_4, high temperatures (>750 °C) [19] are required to achieve high selectivity to CO. During last years, different strategies have been followed to reduce the operation temperature by the using different heterogenous catalysts. For instance, transition metals like Ni, Co and Fe, perovskites or noble metals are widely studied [15,16,20,21]. Zhao et al. [22] optimized a Ni–$CeAl_2O_3$–Al_2O_3/FeCrAl-fiber catalyst with enhanced carbon tolerance for the catalytic oxy-methane reforming (COMR). They found that the achieved performance ~86% CH_4 conversion and ~96.1/~91.5% H_2/CO selectivity was related to the synergism between Ni^0 species and "$CeAl_2O_3$–CeO_2" cycle.

This work was mainly focused on the development of ordered mesoporous materials for its implementation as catalyst for POM as well as anode in the intermediate temperature solid oxide fuel cells (IT-SOFCs). SOFCs anodes need to accomplish a series of requirements as high electrocatalytic activity and stability in reducing environment. One of the main challenges for the ĊPOM is the development of a selective and stable catalyst for its operation at lower temperatures. As a result, the obtained mesoarchitectured materials in the current work were assessed as catalyst for POM in the intermediate temperature range (600–900 °C) and over time. Furthermore, high electronic conductivity and compatibility with other materials of the SOFC system should be fulfilled. Thus, the effect of the Pr, Er and Sr addition to CeO_2 lattice on the structural, textural and surface chemistry properties was investigated. Our aim was focused on doping the CeO_2 mesostructures with trivalent (Pr^{3+}/Er^{3+}) and divalent (Sr^{2+}) cations to generate more defects in the structure and, therefore, a large number of oxygen vacancies. In addition, the presence of the ions with lower valence state such as Sr^{2+} and $Pr^{(+3/+4)}$ as well as the formation of the mesopore structures with uniform pore size distribution play an important role in the transport and electrocatalytic properties. The reason for introducing Sr is its double advantage in terms of its low cost and an enhancement of the bulk electrical conductivity by incorporation with a high dispersion in the fluorite lattice. We have chosen the Sr concentrations (2.5 si 5 mol.%, respectively) based on a previous study of Ali et al. [23]. The aforementioned authors proved the successful incorporation of Sr (3% and 5%, respectively) by a similar coprecipitation method without any template. Our main tasks was to incorporate Sr (with rather low concentrations) into the lattice and to minimize as much as possible the occurrence of SrO secondary phase. Indeed, the significant presence of the trivalent Pr^{3+} and Er^{3+} ions (15 mol.%, overall) could boost the later undesired effect. Thus, we expect an improvement of the oxygen mobility in the bulk as a result of the lattice distortion by incorporation of ions with different radii. 10 wt% Ni was deposited on the nanostructured CeO_2 obtained by a surfactant free solvo-thermal method proving to be active for POM. The deposition procedure involves the cetyltrimethylammonium bromide (CTAB) as morphology controlling agent, the polyvinylpyrrolidone as particle size controlling agent and hydrazine hydrate [$NH_2NH_2 \bullet H_2O$] as reducing agent. The catalyst, reduced before reaction, with 20% H_2 balance He for 2h at 600 °C and diluted with inert γ -Al203 showed a CH_4 conversion ~93%, a CO selectivity ~92% and good stability over time, 20h [24]. Mesoporous ceria, templated by CTAB, obtained by a precipitation method under refluxing conditions was used as support for Ni deposition (2.5–15 wt% Ni) by wetness impregnation technique. It was found that in the temperature range (500–700 °C) the CH_4 conversion remain around 82% and a slightly increased of the H_2/CO ratio was observed. At 800 °C CH_4 is converted at ~78% but a sudden decrease of H_2/CO ratio occurred [25].

In this work, we developed NiO/Sr doped $Ce_{0.85}Pr_{0.10}Er_{0.05}O_{2-o^-}$ (2.5 and 5 mol.% Sr) mesoarchitectured by a facile synthesis protocol with catalytic and electrochemical performance. Our versatile and low cost synthesis procedure offers advantages such as the direct incorporation of ions with lower valence states for the stabilization of the cubic CeO_2 lattice, the formation of the mesoporous structures and leads to the removal of work steps such as the use of hydrazine (highly toxic) as a strong reducing medium for the Ni deposition process as well as the expensive pre-reduction procedures of catalysts by using H_2 in the atmosphere of He. The effect of the composition and the structural, textural and surface chemistry investigations on the catalytic and electrochemical behavior were studied. The materials exhibited a good catalytic performance in the POM and good stability over time. Also, we developed and tested NiO/CPS/YSZ/GDC/Pt electrochemical cells with the anodic side fueled by wet H_2 (2.5% vol. H_2O) Thus, we expect an improvement of the oxygen mobility in the bulk as a result of the lattice distortion by incorporation of ions with different radii, as required for anode applications.

2. Synthesis and characterization

2.1. Synthesis

We approached a preparation protocol for the mesostructured anodes which involved two working stages, as followsi) preparation of mesoporous supports based on Sr doped $Ce_{0.85}Pr_{0.10}$ $Er_{0.05}O_{2-o^-}$ (2.5 and 5 mol.% Sr); ii) NiO deposition by wet impregnation method on the mesoporous supports.

i) Sr doped $Ce_{0.85}Pr_{0.10}$ $Er_{0.05}O_{2-o^-}$ (2.5 and 5 mol.% Sr) with mesoporous structures were synthesized by a hydrothermal route templated by a nonionic surfactant, Triton X100. The non-ionic surfactant was very well dispersed in water under strong stirring conditions for obtaining the micellar solution. The cerium (III) nitrate hexahydrate (Merck), praseodymium (III) nitrate hexahydrate (Merck), erbium trinitrate pentahydrate (Merk) and strontium nitrate ACS reagent, >99.0% (Sigma

Aldrich) inorganic precursors were added. The vigorous stirring was kept for 4 h at room temperature and finally the pH value was adjusted to 12 using tetrabutylammonium hydroxide (TBAOH) solution ~40% in water (Sigma-Aldrich) and left for aging 24h, maintaining the stirring. The obtained solutions were loaded into Teflon liner autoclave equipped with pressure gauge and heated at 160 °C for 48 h, under stirring. The autogenous pressure developed during the hydrothermal treatment was ~5 atm. The mesostructures were obtained by calcining at 600 °C in air for 8h.

ii) 10 mol.% NiO was deposited on mesoporous supports by wet impregnation using a $Ni(NO_3)_2$ aqueous solution. The impregnated powders were dried at room temperature for 12h and thermally treated at 900 °C, in air, for 8h. The NiO/Sr doped $Ce_{0.85}Pr_{0.10}$ $Er_{0.05}O_{2-o}$ materials were labeled **NiO/CPS1 and NiO/CPS2**, corresponding to Sr amount (2.5 and 5 mol.% Sr, respectively)

2.2. Characterization methods

X-Ray diffraction - The structural aspects were assessed using a PANalytical X'Pert PRO diffractometer with CuKα1,2 radiation and an X'Celerator detector in Bragg–Brentano geometry. The measurements were recorded in the 2θ range from 0° to 80°. Cu Kα1,2 radiation and an X'Celerator detector in Bragg–Brentano geometry.

Raman spectroscopy - Raman spectra were obtained by using a Jobin Ivon Raman microprobe instrument, with an excited wavelength of 632 nm laser radiation. All the spectra were recorded between 200 and 1000 cm^{-1} with a × 50 objective which focuses the laser beam in a spot of 100 mm.

Porosity Analysis (BET) – An analyzer ASAP-2020 manufactured by Micromeritics was used for the textural assessment. The Bru- nauer–Emmett–Teller adsorption–desorption isotherms of N_2 were ob- tained at 196 °C in the wide range of 0.01–0.995 relative pressure after degassing at 150 °C overnight.

Scanning electron microscopy (SEM) – The morphological aspects were studied by scanning electron microscopy (SEM) using a Quanta 3D SEM, operating at 10 kV. In order to correlate topographical features in the micrographs and local variations in composition, secondary (SE) and backscattered (BSE) electrons images were recorded simultaneously on selected areas.

X-ray photoelectron spectroscopy (XPS) – The surface chemistry investigations were carried out on PHI Quantera equipment with a pressure in the analysis chamber of 10^{-9} Torr and monochromatized Al Kα radiation (1486.6 eV). The charging effect was minimized by a dual beam (electrons and Ar ions) neutralizer. The calibration of the spectra was performed using the C1s line (BE= 284.8 eV) corresponding to hydrocarbon adsorption from environment.

Temperature programmed reduction (H_2 - TPR) - were conducted on a PoropaQ apparatus under hydrogen atmosphere. Before analysis the powders (~50 mg) were treated in air flow (30 ml min^{-1}) for 1 h at 150 °C. Before reduction the samples were cooled to room temperature in argon gas flow (50 ml min^{-1}). For TPR analysis, was used a gas flow of 5% H_2 in argon at a flow rate of 50 ml min^{-1}. The temperature was increased to 900 °C with a rate of 10 °C min^{-1}.

Catalytic activity measurements - The catalytic activity for partial oxidation of methane was assessed in a continuous fixed-bed tubular reactor (length of 300 mm and i.d. of 9 mm, Hasteloy X tube), equipped with a thermo well in the center of the catalyst bed. The experiments were typically carried out in a downflow system at atmospheric pressure and at the reaction temperatures specified further. The catalyst powder, placed between two layers of quartz wool, was activated before the re- action for 2 h in air, at 800 °C, and then the reactor was cooled down to 200 °C. Catalytic reactions were performed at several temperatures starting from 200 °C, using a feed containing 13.33% CH_4; 6.66% O_2; 80% N_2 at a total flow of 37.5 mL min^{-1} and GHSV of 22500 h^{-1}. The reaction products were examined online by a gas chromatograph from Shimadzu equipped with TCD and FID detectors and two capillary columns Molecular Sieve 5A and Poraplot Q (length, 60 m; internal diameter, 0.32 mm; film thickness, 0.5 μm). Activity and selectivity results were calculated according to the equations given below:

$$CH_4\ conversion\ (\%) = \mu_{CH4in} \quad \mu_{CH4out}/\mu_{CH4in} \times 100 \tag{1}$$

$$CO\ selectivity\ (\%) = \mu_{CO}/\mu_{CH4in} \quad \mu_{CH4out} \times 100 \tag{2}$$

Electrochemical characterization – The **NiO/CPS1 and NiO/CPS2** anode materials were characterized by means of the Electrochemical Impedance Spectroscopy (EIS) technique in 1 atm configuration. For that purpose, screen-printable inks composed of the **NiO/CPS1 and NiO/CPS2** powders and a 6% wt. ethylcellulose-terpineol solution in a 1:1 wt ratio were prepared by mixing them in a three-roll mill. The resulting pastes were screen printed on yttria stabilized zirconia (YSZ) dense electrolyte (15 mm OD). Porous electrodes were obtained after calcining the resulting screen-printed layers at 1050 °C for 2h. A top screen-printed gold mesh was applied on the electrodes to ensure proper current collection. As a counter electrode, platinum paste was applied on the opposite side of the electrolyte, and calcined at the same temperature.

Cells were tested by Electrochemical Impedance Spectroscopy (EIS, using a Solartron 1470E/1455 FRA with an AC potential of 20 mV and a frequency sweep from 0.03 Hz to 1 MHz. The EIS measurements were performed at different operation temperatures (between 550 °C and 800 °C) in wet H_2 (2.5% vol.).

3. Results and discussion

3.1. Structural analysis by X-ray diffraction (XRD) and Raman spectroscopy

The XRD patterns of NiO/CPS samples depicted in Fig. 1 (a), detect the fluorite-type ceria-based structure, cubic NiO, and the formation of Pr sesquioxide as minor phase. CeO_2 with trivalent dopants, such as Pr^{3+} or Er^{3+}, form solid solutions that maintain the cubic fluorite-type structure. Pr doping of ceria has been shown previously to decrease the lattice constant, compared to that of undoped CeO_2 (5.412 Å), effect attributed usually to a mixed (3+/4+) valence, not purely trivalent. Our previous data confirmed the decrease [26]. On the other hand Er leads to the expansion of the lattice [27]. The samples of study contain double the amount of Pr compared to Er, but the effect of Er on the lattice is higher at equal doping [26–28], therefore Er doping can fully offset the effect of the Pr cations on the lattice. The effect of Sr doping on the lattice is very small, Raj Ali et al. [23] have recently reported the same lattice parameters for undoped and Sr-doped CeO_2 with Sr contents of 3 and 5 mol%.

It must be noted that the fluorite type ceria doped phase in CPS2 has smaller lattice parameter (5.394 Å) than in CPS1 (5.404 Å), we attribute this to a higher content of Pr incorporated effectively in the Ce lattice. The ratio Pr/Ce being higher in CPS2, together with very little incor- poration of Sr in the doped lattice, very small features at ~21, ~22, and a doublet at ~25 deg, in the XRD pattern of CPS2, shown in the inset in Fig. 1a. The surface chemistry -discussed bellow- indicates the formation of traces of different Sr and Ce binary oxides (1:1-$SrCeO_3$; 2:1-Sr_2CeO_4 and also 2:2 $Sr_2Ce_2O_5$) [29]. Therefore, additional Sr content in CPS2 seem to form strontium cerates instead of incorporating in the ceria phase.

Ceria crystallite size, calculated using the Debye-Scherrer method, is slightly bigger in CPS2 (18 nm) than in CPS1 (15 nm), while NiO crys- tallite size is significantly bigger when it is deposited on CPS1 than on CPS2 (40 vs 18 nm on CPS2).

There is a single allowed Raman mode in fluorite type dioxides, with F_{2g} symmetry, a mode associated to the O atoms symmetric breathing around the metal cation. The frequency of this mode for CeO_2 is 465 cm^{-1}, and its position is nearly independent of the cation mass. On the other hand, it is affected by the substitution of Ce^{4+} with lower valence

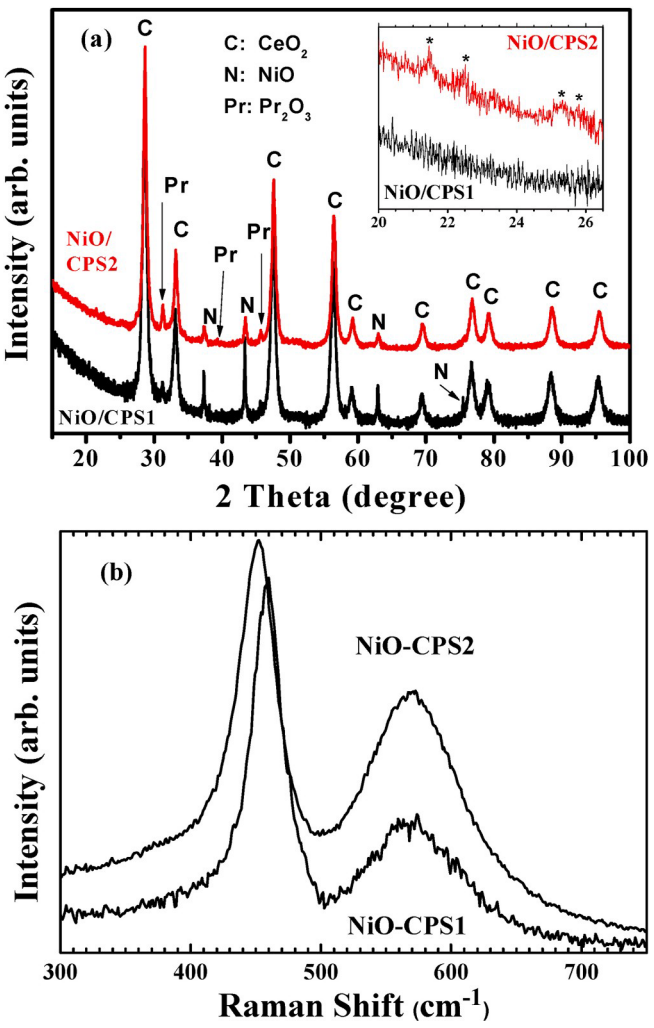

Fig. 1. XRD patterns (a) and Raman Shift (b) for NiO/CPS1 and NiO/CPS2.

cations, that affects the oxygen sublattice by introducing oxygen vacancies. Rare Earth (RE)-doping with trivalent cations thus causes the broadening of the Raman peak and its downshift to lower frequencies. It can be observed in Fig. 1(b) that the pure CeO_2 mode at 465 cm^{-1} shifts to lower frequency: 458 cm^{-1} in CPS1 and 452 in CPS2, indicating an increasing RE doping level [30,31]. In addition, the Raman line broadens and becomes asymmetric with a low frequency tail. Even though, small particle size has been reported to cause the shifting of the CeO_2 strong line to lower energies, accompanied by broadening as the particle size gets smaller [32,33]. We must note that the shift of the CeO_2 mode observed here, cannot be attributed to particle size reduction, as particle size effect is observed for significantly smaller sizes than those of CPS samples. Furthermore, a new broad feature appears in the spectrum at 570 cm^{-1}, with increasing intensity in CPS2. The 570 cm^{-1} band is undoubtedly attributed to oxygen vacancies introduced into the lattice, thus indicates lower valence cation substitution for tetravalent Ce^{4+} [28, 30,34]. It has been reported in Pr-substituted CeO_2, the band intensity being associated with the amount of oxygen vacancies in the substituted lattice [31,35]. Therefore, Raman spectra demonstrate the presence of oxygen vacancies in CPS1 and CPS2 doped lattices and the presence of a higher proportion of oxygen vacancies in CPS2 than in CPS1.

3.2. *Textural assessment by N_2 adsorption/desorption (BET)*

Surface area measurements were determined using BET formalism and confirm the mesoporosity of the NiO/Sr doped $Ce_{0.85-x}Sr_xPr_{0.10}Er_{0.05}$ powders calcined at 900 °C. Indeed, the shape of the adsorption/desorption isotherms is type IV, typical for mesoporous materials- according to the IUPAC classification, with a well-defined hysteresis loop in the range of $0.7<P/P0<0.9$ (Fig. 2a and b).

The obtained surface areas (S_{BET}) show the values of ~22 m^2/g for NiO/CPS1 and ~25 m^2/g for NiO/CPS2. It is worth to notice that these values are quite high considering the high value of the temperature used for calcination (900 °C). The presence of the broader pore distribution was estimated from the Barrett–Joyner–Halenda (BJH) analysis (Fig. 2c and d). Furthermore, it was found that by increasing the Sr content leads to a slight broadening of the pore size distribution. NiO/CPS1 shows an average pore size of about 20 nm while NiO/CPS2 exhibits a broadening in the pore size up to ~30 nm. The broadening effect of the pore size distribution can be explained by the formation of additionally secondary cerates type phases associated with the increasing the Sr content.

3.3. *Morphology by scanning electron microcopy (SEM)*

The microstructure studied by SEM (Figs. 3–4) revealed homogeneous size nanopowders, with intergrain porosity. Correlation between pairs of BSE and SE micrographs taken simultaneously from the same area, showing average atomic weight (Z-contrast) and topographic contrast, respectively, indicate compositional homogeneity and very good mixing of the phases up to the nanoscale.

BSE images reveal the presence of secondary phases only at high magnification, proof of the intimate mixing of CeO_2 and NiO phases achieved using the NiO impregnation method after hydrothermal synthesis of doped ceria nanoparticles. The fine dispersion of the secondary phases is indicated by the lack of Z-contrast. NiO, with an average atomic weight of ~25, is not readily detectable, embedded in the $Ce_{0.85}Pr_{0.10}Er_{0.05}O_{2-\delta}$ (average atomic weight ~59), even at the nanoscale. The observation of the regions with different brightness in BSE images due to Z-contrast reveals that in all cases these regions (hardly detectable, only at high magnification images) are sized below 20 nm. Therefore, the size of NiO clusters can be limited to a scale of less than 20 nm, ruling out the agglomeration of second phase nanocrystallites in any zone of the sample. BSE images reveal to an homogeneous phase distribution, with nanocrystallites of secondary phases well dispersed in close contact with crystallites of the main phase.

3.4. *Surface chemistry characterization by X-Ray photoelectron spectroscopy (XPS)*

The surface element composition (<10 nm) as well as their associated chemical states were assessed by X-ray Photoelectron Spectroscopy. The survey spectra, depicted in Fig. 5a, highlight the presence on the surface of the all elements introduced from inorganic precursors. Ni2p, Ce3d, Pr3d, Er4d and Sr3d most prominent XPS transitions display mainly 2^+, 4^+, 3^+ and 2^+ valence states, respectively (Figs. 5 and 6). It is worth to mention our estimated errors in the Binding Energies (BEs) assignments and quantification assessments (relative concentrations): ±0.2 eV and ±5%, respectively.

From Fig. 5(a–f), 6 (a, b) and Table 1 the following conclusions are drown. Ni is found in its 2+ oxidation state corresponding to NiO (Fig. 5b) in agreement with XRD results. Ce owns 4+ oxidation state mainly as CeO_2 and a rather small amount as cerates (Fig. 5c). A close inspection of Pr3d photoelectron spectra highlighted mainly the presence of Pr^{3+} valence state for both samples, following the values of the binding energies as well as the Pr3d associated satellites and their relative intensities (Fig. 5d). However, a small shoulder at 966.5.2 eV (*) [33] provides evidence about the presence of a tiny amount of 4+ phase for the sample NiO/CPS1. The presence of a tiny amount of Pr^{4+} in the NiO/CPS2 sample cannot be entirely ruled out; however, its presence on the outer surface layer could be hidden by the "shadowing effect" as a result of changes in surface morphology. Er was detected on the surface only as Er^{3+}, most probably inserted in the lattice, either interstitially

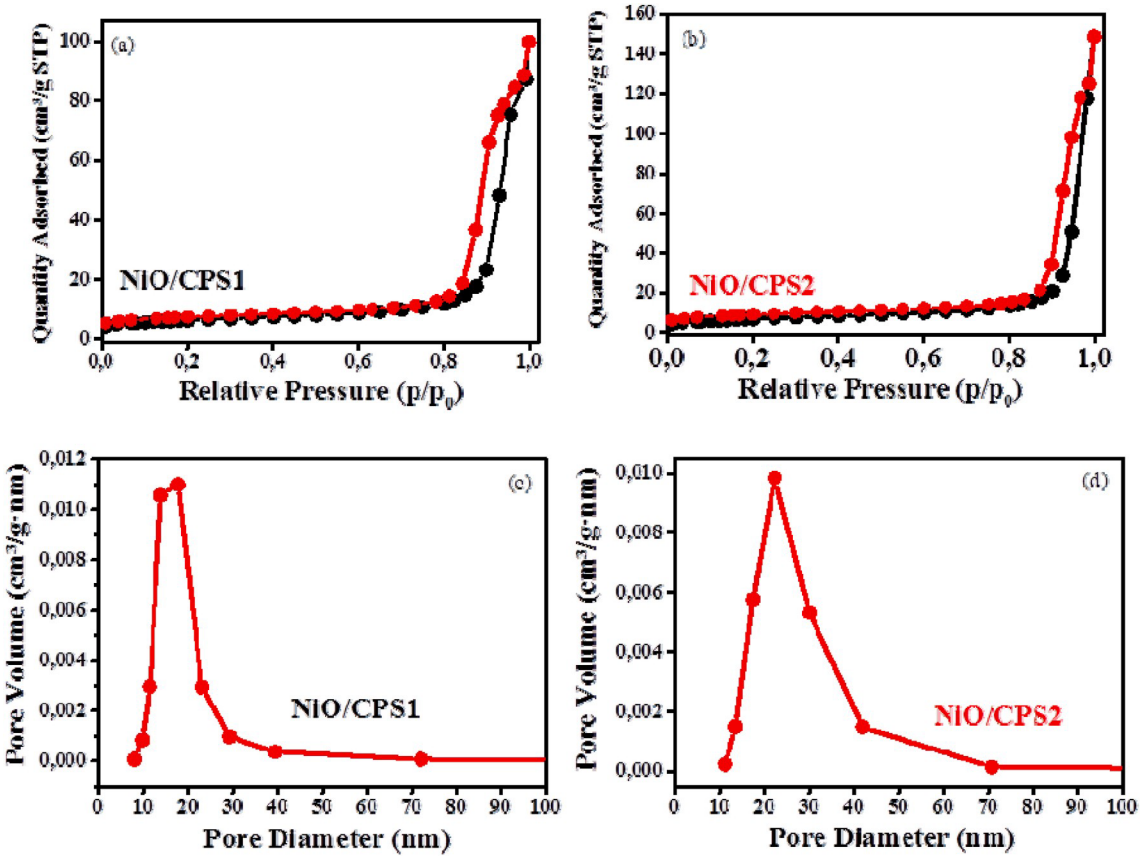

Fig. 2. N_2 adsorption/desorption isotherms (a) and pores size distribution (b).

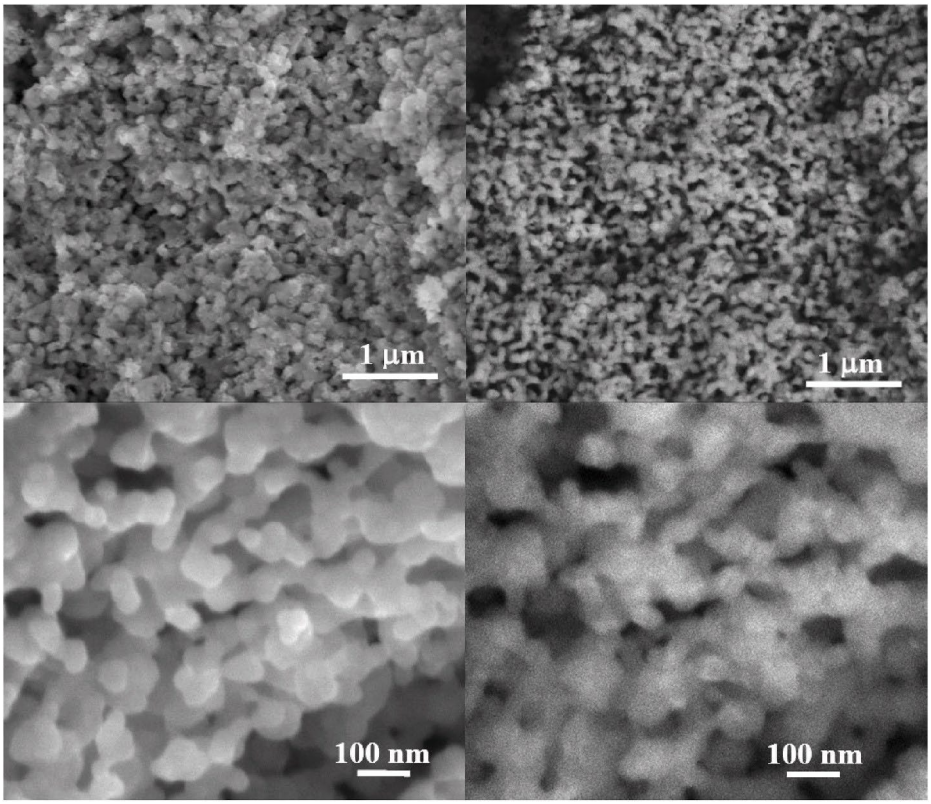

Fig. 3. SEM micrographs for NiO/CPS1 at different magnifications: SE images on the left side and corresponding BSE images on the right side.

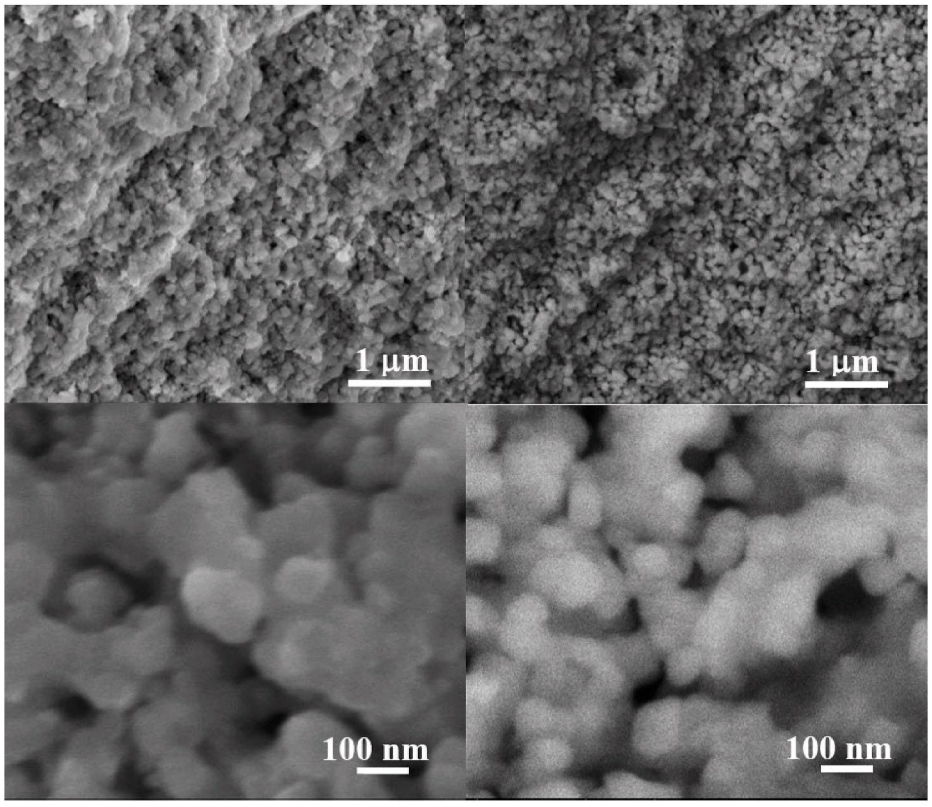

Fig. 4. SEM micrographs for NiO/CPS2 at different magnifications: SE images on the left side and corresponding BSE images on the right side.

located, or substituting tetravalent Cerium.

Sr 3d band-like spectra (Fig. 6 and Table 1) exhibit a complex structure suggesting a key role in surface chemistry. Thus, after the deconvolution procedure the following chemical species were detected: I) Sr^{2+} incorporated into a fluorite ceria lattice. This is the major phase for both samples (see Table 1); II) Sr^{2+} in $SrCeO_3$ and III) a mixture of other kind of cerates such as Sr_2CeO_4 and $Sr_2Ce_2O_5$ as minor phases.

The associated numerical values are given in Table 1.

*) The instrumental resolution easily allows the splitting of the Sr3d doublet but the band – like shape suggests the presence of the superimposed chemical states.

The shape of Ce4d spectra (Fig. 5e) strengthens this statement.

The aforementioned chemical species are related to the content of Sr in the samples. A lower amount of Sr incorporated by the direct synthesis protocol leads to a major phase of Sr^{2+} embedded into the fluorite matrix (~81%). The remaining (~19%) corresponds to Sr bonded into cerates type phase showing a chemical shift of ~1.0 eV towards higher BEs. By increasing the amount of Sr some structural modifications occur induced by the formation of a more pronounced cerates type phase confirmed by the XRD results and also found on the outermost surface layer. The sample NiO/CPS2 also displays a tiny amount of a mixture $Sr_2CeO_4/Sr_2Ce_2O_5$ (Table 1). After the quantitative assessment (see Table 1) one can notice that the increasing of Sr content favors the growing of the cerates phase on the surface at the expense of decreasing the amount of Sr incorporated into the cubic fluorite type lattice. The latter could be a result of the segregation/diffusion process promoted by the structural reorganization according to the XRD indexing. Thus, the XPS findings are in agreement with the XRD results leading to data consistency. In line with this statement, we calculated in addition the ratios (Pr/Ce) for the samples CPS1 and CPS2, finding a higher value for the sample CPS2 as compared to CPS1, in agreement with the intended values and XRD results.

The surface composition assessed by X-Ray Photolectron Spectroscopy, from HR spectra, is shown in Table 2. It is worth to mention that the experimental errors in XPS data quantification is in the range of ±10%. With a roughly 12 atom % contribution from the unavoidable carbon that results from the hydrocarbon adsorption from environment, we should make a comparison with our nominal stoichiometry.

While Ni content is found close to the nominal value percentage (~20 atom %, equivalent to ~ 10 wt%) differences can be noticed for the Sr and rare earth relative concentrations. Thus, higher experimental values were obtained for Sr and Pr at the expense of lower Ce and Er relative concentrations. Roughly, the content of Sr detected on the outermost surface layer is two times higher than the nominal values. The same tendency can be observed in CPS1/CPS2 support samples. These findings can be explained by a segregation process of Sr and Pr from the bulk to the surface accompanied by a diffusion of Ce and Er from the surface to the bulk. Thus, the outermost surface layer appears as enriched in Sr and Pr.

3.5. Temperature-programmed reduction (H_2-TPR) -

The reducibility of the prepared Ni/CPS1, NiO/CPS2 anodes as well as of the CPS1 and CPS2 supports was evaluated by H_2-TPR measurements and the reduction profiles are depicted in Fig. 7a and b. The profiles consist into two reduction regions: low and high temperature, respectively.

The low temperature region (<500 °C), exhibits two majors reduction peaks at around 350 and 460 °C attributed to the reduction of Ni^{2+} and Ce^{4+} surface species [36,37]. The contribution of the reduction of Pr^{4+} species cannot be entirely ruled out as its presence was suggested by X-ray diffraction and XPS analysis and our results are consistent with literature data [35]. A shift to lower temperatures is observed for CPS1 sample that contains a lower amount of Sr suggesting a higher oxygen surface mobility and a better reducibility for this sample.

It is worth to mention that our goal was to have a high dispersion of NiO and also to create a strong interaction between NiO and the ionically conducting matrix, during the thermal treatment at 900 °C. Indeed,

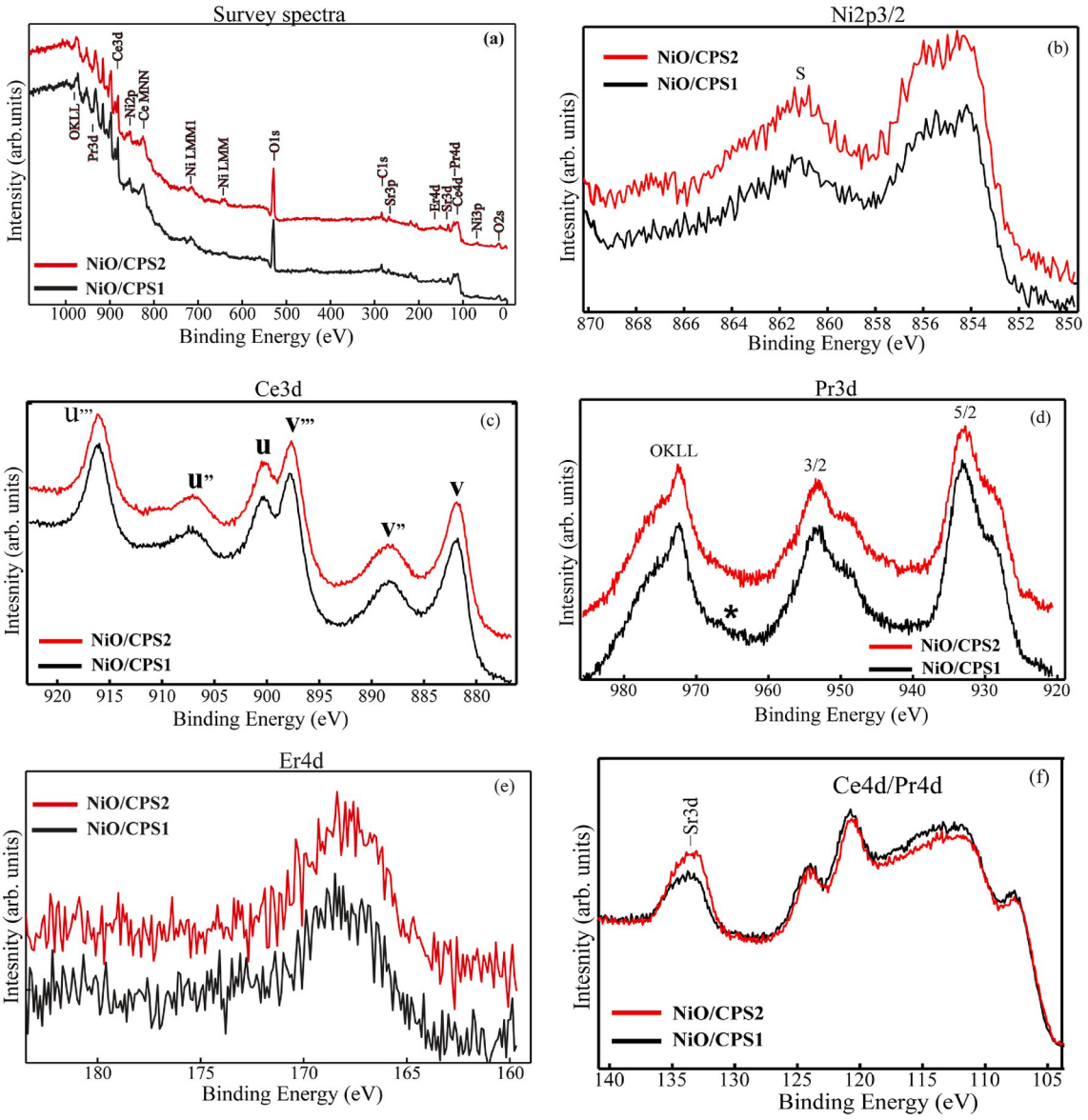

Fig. 5. Survey spectra (a), Ni2p (b), Ce3d (c), Pr3d (d), Er4d (e) and Ce4d/Pr 4d (f) high resolution, superimposed XPS spectra. The associated numerical values are found in Tables 1 and 2

in the high temperature region, the reduction peak at 630 °C can be assigned to the reduction of nickel, existing in a strong interaction within the solid solution [6]. The peak is present for both samples at the same temperature.

Both samples based NiO present an intense reduction peak at about 800 °C which may be appointed to the reduction of Ce^{4+} bulk species. However, a small shift (~10 °C) to higher temperature is recorded for NiO/CPS1 sample. In both cases, this reduction temperature is lower than the one presented in pristine CeO_2, indicating a higher oxygen mobility for the doped samples [6]. The oxygen mobility is related to formation of O^2 vacancies in the doped CeO_2 due to the presence of Pr^{3+}, N^{2+}, Er^{3+}, into the CeO_2 lattice (Ce^{4+}), in order to maintain the balance of the electric charge required after the introduction of dopants with a lower valence.

The behavior of the supports in the reducing atmosphere is mainly similar to the anodes obtained after Ni deposition (see Fig. 7b). Thus, for both supports the reduction of the Ce^{4+} surface species takes place at 468 °C, while the Ce^{4+} bulk species are reduced at lower temperatures ~800 °C for CPS1 and ~735 °C for CPS2 in comparison with the anodes based nickel. This shift towards lower temperature is most probably due to the presence of the different Ce^{4+} species coordinated in the fluorite and cerate symmetries, as it was revealed by XRD and XPS methods. A small reduction peak at 581 °C that occurred only for CPS2, could be ascribed to the reduction of some species located very close to the surface..

3.6. *Catalytic properties*

The catalytic properties of as-prepared materials were assessed in the catalytic partial oxidation of methane (POM) and the results are gathered in Fig. 8. To detect the occurrence of homogeneous reactions, blank tests were performed in the presence of quartz wool alone, by using the same reaction parameters as during the catalyst screening, and no methane conversion was recorded. The methane conversion values were taken after 30 min of reaction at each temperature. Products of methane oxidative coupling (C2 and higher hydrocarbons) were not observed on the entire temperature range studied. Both materials were active at intermediate temperature range (600–800 °C) in POM. At 800 °C almost all methane is converted (~93%), with a good selectivity to CO, higher than 90%. Small difference in the methane conversion is observed for

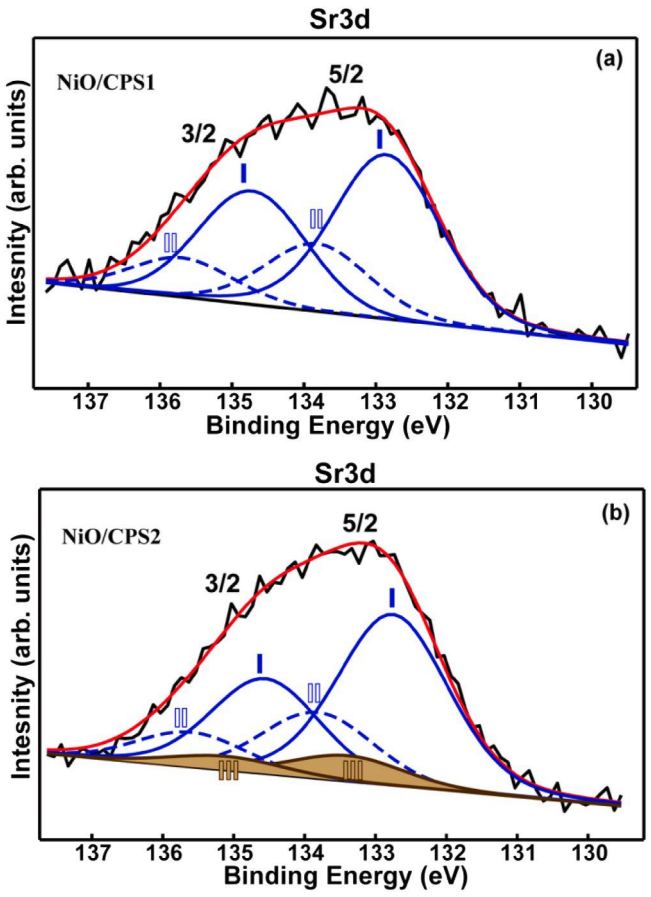

Fig. 6. Sr3d deconvoluted XPS spectra for NiOCPS1 and NiOCPS2 samples.

Table 1
XPS data: the binding energies (BEs-eV) associated to Ni2p3/2, Pr3d5/2 and Er4d photoelectron lines as well as Sr3d chemical state relative concentrations (%).

Sample	Binding energy, eV			
	Ni-2p3/2	Pr3d5/2	Er4d	Sr (3d5/2; 3d3/2)
NiO/CPS1	854.2	932.2	168.3	I - 132.8; 134.6–80.9% II -133.8; 135.6–19.1%
NiO/CPS2	854.3	932.3	168.1	I - 132.8; 134.6–66.8% II - 133.8; 135.6–23.8% III - 133.4; 135.1–9.4%

*) The BEs of the (v,u) features for Ce3d spectra(Fig. 5b) and the overall shape of the spectra as well, provide clear evidence of the pure Ce(4+) oxidation state. The fingerprints (v', u') at 885.4 eV and 904.1 eV, respectively characteristic to 3+ oxidation states are completely vanished.

Table 2
XPS quantitative data.

Sample	Atomic and cation relative concentrations (atom%)					
	O	Ni	Sr	Ce	Pr	Er
NiO/CPS1	68.2	7.0	2.2	16.4	5.4	0.8
		21.7	6.4	51.7	17.6	2.6
Ni/CPS2	69.8	6.8	3.1	14.8	4. 7	0.8
		21.1	10.2	49.6	16.8	2.3
CPS1 Support	68.7	–	2.2	22.8	5.1	1.2
			7.0	72.8	16.2	4.0
CPS2 support	67.7	–	3.0	22.2	6.0	1.1
			9.0	69.0	18.1	3.9

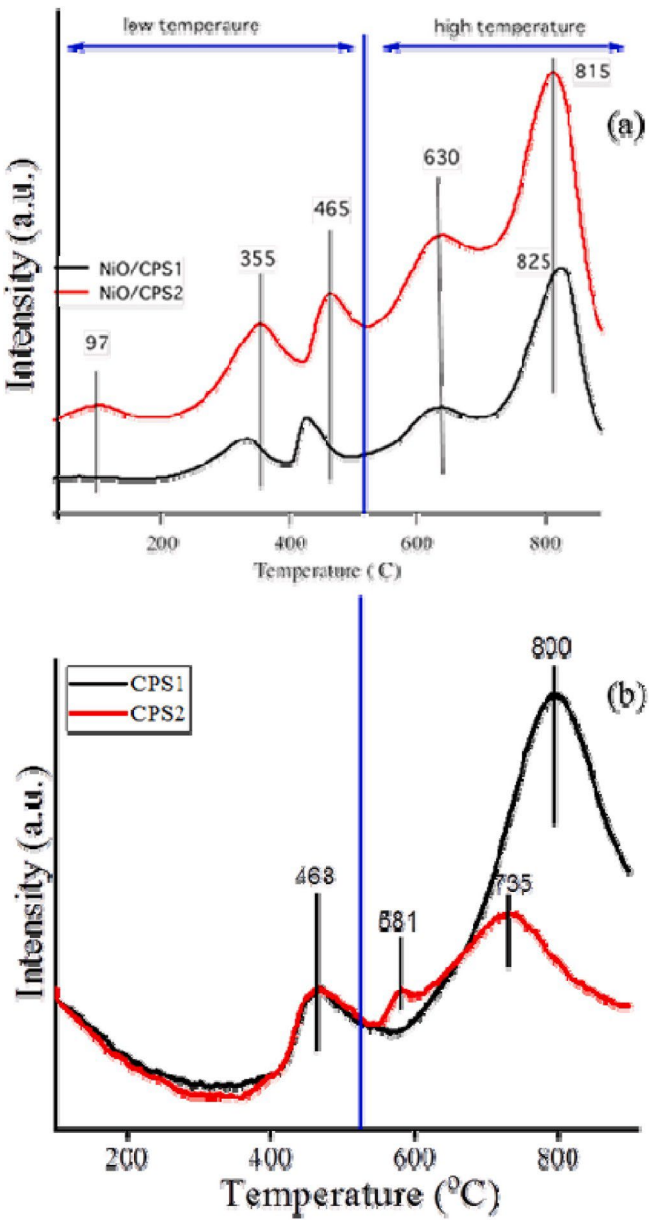

Fig. 7. H_2-TPR profiles of NiO supported on CPS1 and CPS2 samples (a) as well as of CPS1/CPS2 supports (b).

the two studied sample; NiO/CPS1, containing a lower Sr loading, being more active than NiO/CPS2. This can be correlated with H_2-TPR data that indicate a higher oxygen mobility and implicitly a better reducibility for NiO/CPS1 sample. However, it should be mentioned that X-ray diffraction data showed that additional Sr content in CPS2 seem to form strontium cerates instead of incorporating in the ceria phase, this being detrimental, in a small extent, to the catalytic activity.

The catalytic tests over time, depicted in Fig. 8 (b) were performed by directly ramping to 850 °C without passing through intermediate temperatures, using a stoichiometric CH_4/O_2 feed ratio of 2 at a GHSV of 22500 h^{-1}. NiO/CPS1 sample loose ~3% of methane conversion in the first 400 min and after that both materials are stable with time on stream, indicating that the Sr loading does not influence the material stability.

According to eq (1) the reaction products obtained by the partial oxidation of CH_4 are CO and H_2 in a ratio of 1–2. As we observed among the reaction products besides CO occurs also CO_2 and, consequently, we assume that the total oxidation of CH_4 takes places according with eq

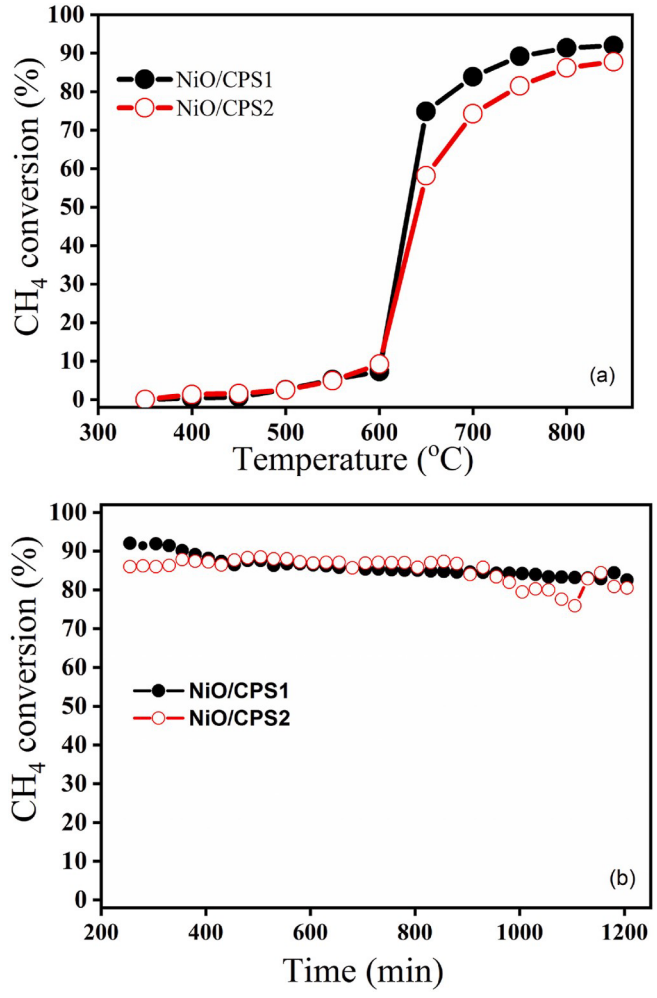

Fig. 8. Catalytic partial oxidation of methane at different temperature (a). and over time at 850 °C.

(2).

$CH_4 + 1/2O_2 \rightarrow CO + 2H_2$ (1)

$CH_4 + 2O_2 \rightarrow CO_2 + 2H_2O$ (2)

Fig. 9a–d depict the evolution in time of CO and CO_2 selectivities for the studied samples in POM at different temperatures. The selectivity of CO increases with the reaction temperature, in detriment of CO_2 formation, as thermodynamically expected. At 850 °C the syngas production became the principal reaction. The selectivity profiles do not depend, in this case, on the material composition. Concerning the CO selectivity as a function of temperature, it is worth to notice that a dependence on the material composition is highlighted in the temperature range (650–850)°C. Thus, the formation of CO starts at 650 °C with a selectivity of 78.8% for NiO/CPS1 and 66.5% for NiO/CPS2, respectively and reaches a selectivity of ~95% at 850 °C for both samples. This behaviour could be related to the Sr incorporation in the lattice as well as to an enrichment in Sr and Pr of the outermost surface layer, as it was proved by XPS.

3.7. Electrochemical properties -

Finally, the mesoporous materials were characterized as anode under reducing conditions. Yttria stabilized zirconia (YSZ) was selected as electrolyte material to avoid the leakage of electrons, which previously has been observed in other electrolyte materials for operation under reducing atmospheres [38], whereas Pt was selected as counter electrode. The polarization resistance results obtained by means of the Electrochemical Impedance Spectroscopy in wet H_2, from 800 °C to 550 °C are shown in the Table 3 and Fig. 10.

The Polarization Resistance (Rp) results include the contribution of both electrodes; i.e. Pt and NiO/CPS1or NiO/CPS2 electrodes. Since the cell configuration is the same for both samples (Pt-GDC-YSZ-NiO/CPSX, X =1,2), the difference observed in performance for both anode materials should be mainly ascribed to the NiO/CPS1 and NiO/CPS2 contribution. As can be inferred from the graph, the compound which shows the lowest Sr content in the structure (NiO/CPS1) exhibits also the lowest Rp. The spectrum of both anode materials at 600 °C obtained by Electrochemical Impedance Spectroscopy has been plotted in Fig. 11. The real resistance associated mainly to the electrolyte material has been subtracted in the Nyquist plot (Fig. 11a) to compare directly the resistances of both electrodes. As can be inferred from Fig. 11b NiO/CPS2 exhibits a bigger resistance at medium frequencies, whereas in NiO/CPS1 two different resistances can be perfectly distinguished at high (935 Hz) and medium frequencies (110 Hz). In order to shed further light into the different behavior observed for both electrodes, the electrochemical spectra have been fitted with an equivalent electrical circuit. The selected equivalent circuit (Fig. 11c) consisted in a real resistance and three resistances in series, each of them with a Constant Phase Element (CPE) in parallel, i.e. $R\text{-}R_{HF}/CPE_{HF}\text{-}R_{MF}/CPE_{MF}\text{-}R_{LF}/CPE_{LF}$. The High Frequency (HF) resistance presents an associated pseudo-capacitance in the range of 10^{-5} F cm^{-2} for both materials and it has been previously assigned to electron and ion transfer processes corresponding to the charge transfer resistance occurring at the interfaces [38,39]. The lowest resistance obtained for NiO/CPS2 can be related with the higher oxygen vacancy generation in the fluorite structure, due to the incorporation of higher amount of Sr with a fixed oxidation state of +2 and the oxidation state of Pr (3) determined by XPS. Whereas the Low Frequency arc (LF), with a relaxation frequency of 2–4 Hz can be related with the processes occurring close the Triple Phase Boundary [40]. If the TPB length in the Pt counter electrode is the same for both materials, i.e., the same material and sintering conditions, the lower resistance of NiO/CPS2 would be related with the bigger available TPB length in the electrode. The expected bigger pore size and area BET of NiO/CPS2 leads to a better Ni dispersion and larger active area for the oxidation of hydrogen. Primdahl et al. [41] reported a big reduction of the LF arc associated with the incorporation of a very small amount of Ni in the $Ce_{0.9}Gd_{0.1}O_{1.95}$/Ni electrode, and since the same amount of Ni is present in the studied electrodes, the small difference in the resistance could be ascribed to the better Ni dispersion.

The medium frequency (MF) resistance has been described previously as Ce-based materials dependent and it could be related with the oxidation of the dissociated hydrogen ($2H + O^{2-} \rightleftarrows H_2O$ 2e) on the surface of the ceria material [42]. This process limits the electrochemical performance of both materials, but NiO/CPS1 with Sr incorporated in the lattice enhance the electrochemical oxidation reaction step accompanied with the charge transfer.

4. Conclusions

We have successfully synthesized efficient and cost-effective mesoarchitectures with novel compositions based on NiO/Sr doped $Ce_{0.85}Pr_{0.10}$ $Er_{0.05}O_{2-\delta}$ (2.5 and 5 mol.%) and assessed the catalytic and electrochemical performance. The synthesis protocol involved a hydrothermal route templated by a non-ionic surfactant -Triton X100. Structural evaluation by XRD and Raman spectroscopy revealed a mainly cubic fluorite phase with some traces of Pr_2O_3 and Sr cerates. The textural assessment confirmed the formation of the mesoporous structures at 900 °C with the average pore size in the range (20–30) nm. The XPS investigation on surface chemistry reveals the presence of Er^{3+}, Pr^{3+} oxidation states in the ceria containing only Ce^{4+} ions, leading to oxygen vacancies and enhancing the oxygen mobility. On the other

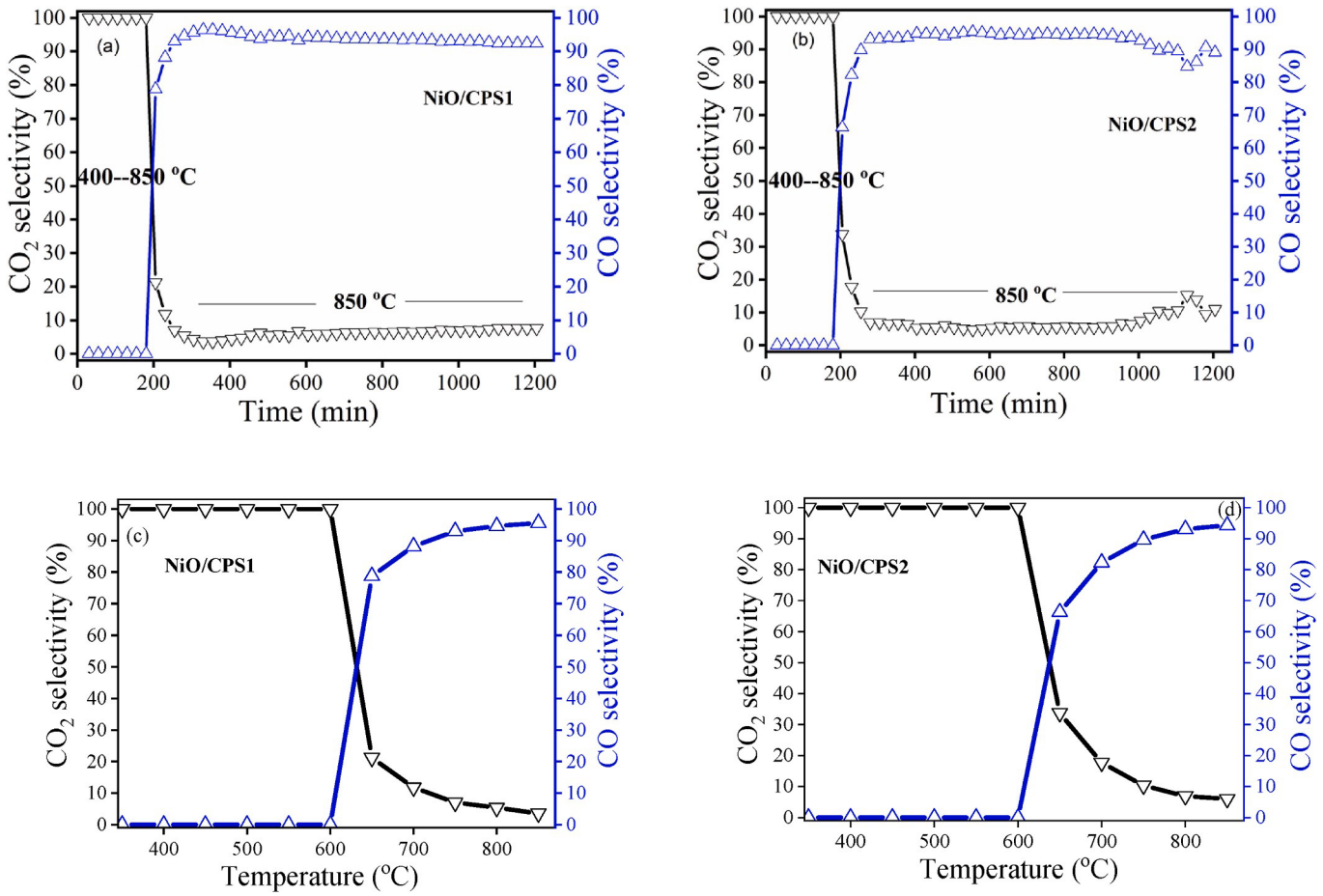

Fig. 9. CO and CO_2 selectivities on NiO/CPS1 (a) and NiO/CPS2 (b) over time at 850 °C and as a function of temperature in the range 350–850 °C (c, d) (CH_4/O_2 =2 at a GHSV of 22.500 h^{-1}).

Table 3
Results of the equivalent circuit fitting at 600 °C in wet hydrogen.

Electrode	T [°C]	RHF [Ω·cm^2]	CHF [F·cm^{-2}]	fHF [Hz]	RMF [Ω·cm^2]	CMF [F·cm^{-2}]	fMF [Hz]	RLF [Ω·cm^2]	CLF [F·cm^{-2}]	fLF [Hz]
NiO/CPS1	600	6.48	$2.62\cdot10^{-5}$	935	19.76	$7.32\cdot10^{-5}$	110	6.29	0.0062	4
NiO/CPS2	600	1.11	$8.23\cdot10^{-5}$	1728	38.27	$1.41\cdot10^{-5}$	29	5.22	0.0135	2

hand, the detected Ni^{2+} highly dispersed and strongly interacting with the support confirmed by SEM and TPR analysis as well as the presence of Sr^{2+} boost the electronic conductivity. The strontium chemistry assessed by XPS highlighted the presence of Sr mainly incorporated in the lattice and a lower fraction coordinated in Sr cerates, in good agreement with XRD and Raman results. The applicability of these materials was checked by testing them as catalysts in ЄPOM with a remarkable CH_4 conversion and selectivity to CO at intermediate temperature range (600–900 °C) and excellent stability over time. It is worth to mention that in the range (600–750 °C), the NiO/CPS1 catalyst with Sr mainly inserted in the lattice (~81%), exhibits a superior CH_4 conversion. We developed the electrochemical cells with NiO/Sr doped $Ce_{0.85}Pr_{0.10}$ $Er_{0.05}O_{2-o}$- mesoarchitectured on the anodic side fueled by wet H_2 (2.5% vol. H_2O) and yttria stabilized zirconia (YSZ) as electrolyte together with gadolinium doped ceria (GDC) as buffer layer. An enhancement of the electrochemical properties was observed for the NiO/CPS1 anode which exhibits a lower resistance with two perfectly distinguished values at high (935 Hz) and medium frequencies (110 Hz). This complex impedance behavior may be related to intrinsic electrocatalytic activity, a stronger activation by the desirable cations with lower valence states able to stabilize the cubic ceria. We envisage to further tailor the anodes aiming to boost the electrocatalytic properties depending on the type of fuel, electrolyte, the choice of cathode and working temperature.

CRediT authorship contribution statement

Laura Navarrete: Conceptualization, Methodology, Writing - Review & Editing, Writing – review & editing, Project administration, Funding acquisition. **Mihaela Florea:** Electrochemical investigations, Investigation, Writing- Original draft preparation, Writing – original draft. **Petre Osiceanu:** Catalytic investigations, Investigation, Writing – original draft. **Jose Maria Calderon-Moreno:** XPS investigations, Investigation, Writing- Original draft preparation, Writing – original draft. **Mihaela M. Trandafir:** XRD, Raman SEM investigations, Investigation, Writing- Original draft preparation, Writing – original draft. **Simona Somacescu:** Catalytic investigations, Investigation. **Jose Manuel Serra:** Conceptualization, Writing - Review & Editing, Writing – review & editing.

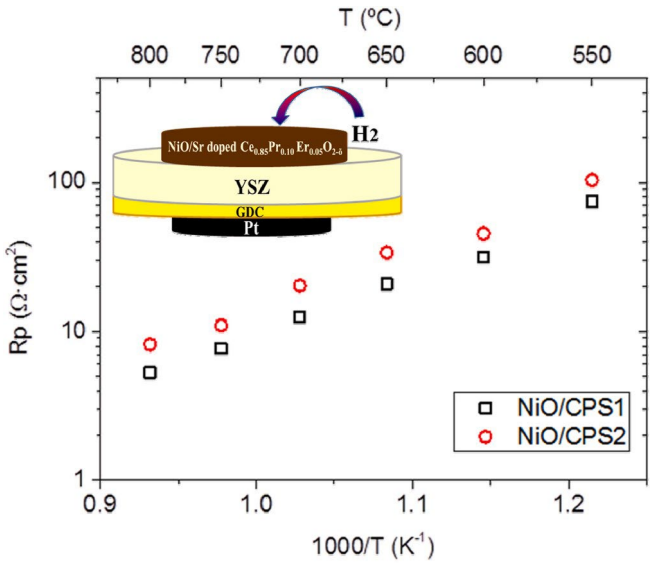

Fig. 10. Polarization resistance results as function of temperature in wet (2.5% vol.) H_2.

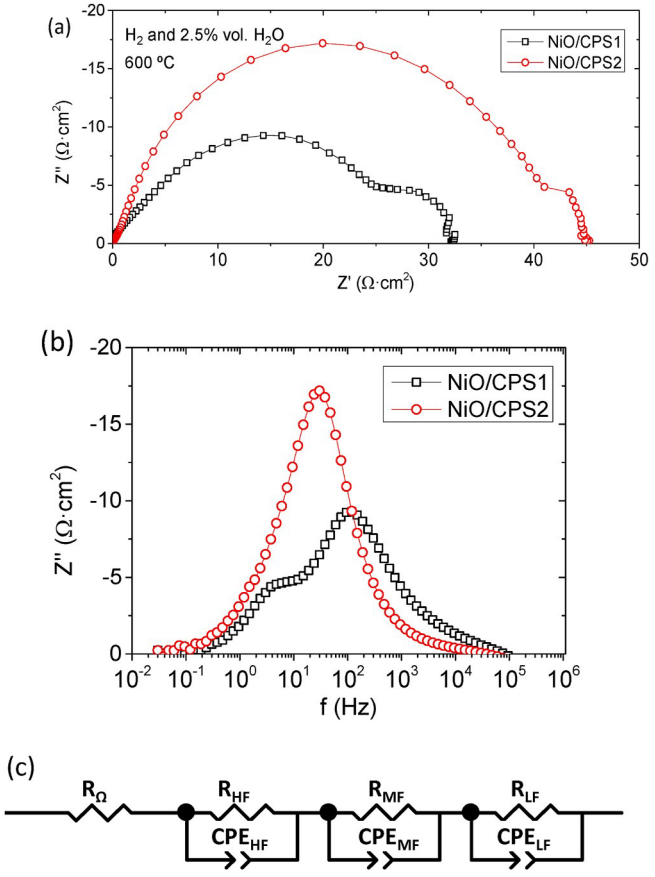

Fig. 11. Electrochemical Impedance spectra of Pt/YSZ and NiO/CPS1 or NiO/CPS2 cells in wet (2.5% vol. H_2O) H_2 at 600. (a) Nyquist and (b) Bode plot and (c) Equivalent Electrical Circuit selected for the EIS fitting.

Declaration of competing interest

The authors declare that they have no known competing financial interests or personal relationships that could have appeared to influence the work reported in this paper.

Acknowledgements

This work was supported by a grant of Partnerships in priority S&T domains Program (PNII), MEN-UEFISCDI, project number 26/2012. MF, MMT. PO, JMCM and SS aknowledge CCCDI – UEFISCDI, project nos 110 and 111/2019, ERANET-M.-CATALEAST, within PNCDI III.

References

[1] A.I. Osman, J. Meudal, F. Laffir, J. Thompson, D. Rooney, Appl. Catal. B Environ. 212 (2017) 68–79.
[2] X. Xu, C. Xia, G. Xiao, D. Peng, Solid State Ionics 176 (2005) 1513–1520.
[3] M.G. Zimicz, F.D. Prado, D.G. Lamas, S.A. Larrondo, Appl. Catal. Gen. 542 (2017) 296–305.
[4] Z. Wang, S. Wang, S. Jiao, W. Weng, K. Cheng, B. Qian, H. Yu, Y. Chao, J. Alloys Compd. 702 (2017) 186–192.
[5] A. Fuerte, R.X. Valenzuela, M.J. Escudero, Univers J Electr Electron Eng 5 (2017) 45–55.
[6] S. Somacescu, N. Cioatera, P. Osiceanu, J.M. Calderon-Moreno, C. Ghica, F. Neat¸u, M. Florea, Appl. Catal. B Environ. 241 (2019) 393–406.
[7] Y. Su, D. Lu, S. Wang, Powder Diffr. 35 (2020) 23–30.
[8] M.G. Bellino, D.G. Lamas, N. Walso¨e de Reca, Adv. Funct. Mater. 16 (2006) 107–113.
[9] N. Jaiswal, S. Upadhyay, D. Kumar, O. Parkash, J. Power Sources 222 (2013) 230–236.
[10] I. Gavrielatos, V. Drakopoulos, S.G. Neophytides, J. Catal. 259 (2008) 75–84.
[11] T. Takeguchi, R. Kikuchi, T. Yano, K. Eguchi, K. Murata, Catal. Today 84 (2003) 217–222.
[12] T. Hibino, A. Hashimoto, M. Yano, M. Suzuki, M. Sano, Electrochim. Acta 48 (2003) 2531–2537.
[13] Y. Ling, Z. Wang, Z. Wang, R. Peng, B. Lin, W. Yu, T.T. Isimjan, Y. Lu, Science China Materials 58 (2015) 204–212.
[14] J. Qu, W. Wang, Y. Chen, X. Deng, Z. Shao, Appl. Energy 164 (2016) 563–571.
[15] A. Emamdoust, V. La Parola, G. Pantaleo, M. Testa, S.F. Shayesteh, A. Venezia, J. Energy Chem. 47 (2020) 1–9.
[16] A.I. Osman, Chem. Eng. Technol. 43 (2020) 641–648.
[17] S. Sengodan, R. Lan, J. Humphreys, D. Du, W. Xu, H. Wang, S. Tao, Renew. Sustain. Energy Rev. 82 (2018) 761–780.
[18] K. Otsuka, Y. Wang, E. Sunada, I. Yamanaka, J. Catal. 175 (1998) 152–160.
[19] E. Kikuchi, Y. Chen, Studies in Surface Science and Catalysis, 1998, pp. 441–446.
[20] A. Lo´pez-Ortiz, M. Mel´endez-Zaragoza, J.S. Guti´errez, P. Gonz´alez-Vargas, V. Collins-Martínez, Int. J. Hydrogen Energy 44 (2019) 12315–12323.
[21] B.C. Enger, R. Lødeng, A. Holmen, J. Catal. 262 (2009) 188–198.
[22] G. Zhao, R. Chai, Z. Zhang, W. Sun, Y. Liu, Y. Lu, Fuel 258 (2019) 116102.
[23] S.R. Ali, R. Kumar, A. Kalam, A.G. Al-Sehemi, M.C. Arya, Arabian J. Sci. Eng. 44 (2019) 6295–6302.
[24] R.K. Singha, A. Shukla, A. Yadav, L.S. Konathala, R. Bal, Appl. Catal. B Environ. 202 (2017) 473–488.
[25] M. Peymani, S.M. Alavi, M. Rezaei, Int. J. Hydrogen Energy 41 (2016) 6316–6325.
[26] S. Somacescu, V. Parvulescu, J.M. Calderon-Moreno, S.-H. Suh, P. Osiceanu, B.-L. Su, J. Nanopart. Res. 14 (2012) 1–17.
[27] S. Chahal, A. Kumar, P. Kumar, Appl. Nanosci. (2020) 1–13.
[28] J. McBride, K. Hass, B. Poindexter, W. Weber, J. Appl. Phys. 76 (1994) 2435–2441.
[29] J. Yuan, H. Zhang, X. Zhou, J. Sun, J. Wang, S. Dong, J. Jiang, L. Deng, X. Cao, Corrosion Sci. 145 (2018) 295–306.
[30] M. Guo, J. Lu, Y. Wu, Y. Wang, M. Luo, Langmuir 27 (2011) 3872–3877.
[31] A. Nakajima, A. Yoshihara, M. Ishigame, Phys. Rev. B 50 (1994) 13297.
[32] J.E. Spanier, R.D. Robinson, F. Zhang, S.-W. Chan, I.P. Herman, Phys. Rev. B 64 (2001) 245407.
[33] S. Somacescu, V. Parvulescu, J.M. Calderon-Moreno, S.-H. Suh, P. Osiceanu, B.-L. Su, J. Nanoparticle Res. 14 (2012) 885.
[34] Z. Wu, M. Li, J. Howe, H.M. Meyer III, S.H. Overbury, Langmuir 26 (2010) 16595–16606.
[35] M. Florea, G. Postole, F. Matei-Rutkovska, A. Urda, F. Neat¸u, L. Massin, P. Gelin, Catalysis Science & Technology 8 (2018) 1333–1348.
[36] C. Rotaru, G. Postole, M. Florea, F. Matei-Rutkovska, V. P^arvulescu, P. Gelin, Appl. Catal. A: Gen 494 (2015) 29–40.
[37] A. Trovarelli, Catal. Rev. 38 (1996) 439–520.
[38] A. Torabi, T.H. Etsell, J. Power Sources 225 (2013) 51–59.
[39] S.B. Adler, Solid State Ionics 111 (1998) 125–134.
[40] D. Burnat, G. Nurk, L. Holzer, M. Kopecki, A. Heel, J. Power Sources 385 (2018) 62–75.
[41] S. Primdahl, M. Mogensen, Solid State Ionics 152 (2002) 597–608.
[42] H. Kishimoto, K. Yamaji, T. Horita, Y.-P. Xiong, M.E. Brito, M. Yoshinaga, H. Yokokawa, Electrochemistry 77 (2009) 190–194.